Performance of the MISR LAI and FPAR algorithm: a case study in Africa

Jiannan Hu[a,*], Bin Tan[a], Nikolay Shabanov[a], Kathleen A. Crean[b], John V. Martonchik[b],
David J. Diner[b], Yuri Knyazikhin[a], Ranga B. Myneni[a]

[a]Department of Geography, Boston University, 675 Commonwealth Avenue, Boston, MA 02215, USA
[b]Jet Propulsion Laboratory, Pasadena, CA 91109, USA

Abstract

The Multi-angle Imaging SpectroRadiometer (MISR) instrument is designed to provide global imagery at nine discrete viewing angles and four visible/near-infrared spectral bands. The MISR standard products include green leaf area index (LAI) of vegetation and fraction of photosynthetically active radiation absorbed by vegetation (FPAR). These parameters are being routinely processed from MISR data at the Langley Atmospheric Sciences Data Center (ASDC) since October 2002. This paper describes the research basis for transitioning the MISR LAI/FPAR product from beta to provisional status. The quality and spatial coverage of MISR land surface reflectances that are input to the algorithm determine the quality and spatial coverage of the LAI and FPAR products. Therefore, considerable efforts have been expended to analyze the performance of the algorithm as a function of uncertainties of MISR surface reflectances and to establish the convergence property of the MISR LAI/FPAR algorithm, namely, that the reliability and accuracy of the retrievals increase with increased input information content and accuracy. An additional objective of the MISR LAI/FPAR algorithm is classification of global vegetation into biome types—information that is usually an input to remote sensing algorithms that use single-angle observations. An upper limit of uncertainties of MISR surface reflectances that allows discrimination between biomes, minimizes the impact of biome misidentification on LAI retrievals, and maximizes the spatial coverage of retrievals was estimated. Algorithm performance evaluated on a limited set of MISR data from Africa suggests valid LAI retrievals and correct biome identification in about 20% of the pixels, on an average, given the current level of uncertainties in the MISR surface reflectance data. The other 80% of the LAI values are retrieved using incorrect information about the type of biome. However, the use of multi-angle data minimizes the impact of biome misidentification on LAI retrievals; that is, with a probability of about 70%, uncertainties in LAI retrievals due to biome misclassification do not exceed uncertainties in the observations. We also discuss in depth the parameters that characterize LAI/FPAR product quality—such as quality assessment (QA) that is available to the users along with the product. The analysis of the MISR LAI/FPAR product presented here demonstrates the physical basis of the radiative transfer algorithm used in the retrievals and, importantly, that the reliability and accuracy of the retrievals increase with increased input information content and accuracy. Further improvements in the quality of MISR surface reflectances are therefore expected to lead to LAI and FPAR retrievals of increasing quality.
© 2003 Elsevier Inc. All rights reserved.

Keywords: MISR; FPAR; Visible/near-infrared spectral bands

1. Introduction

The Multi-angle Imaging SpectroRadiometer (MISR) is an instrument on board the EOS Terra platform. MISR collects observations of the Earth's surface at 1.1-km spatial resolution with the objective of providing atmospherically corrected reflectance properties of most of the land surface and the tropical ocean (Diner et al., 1998; Martonchik et al.,

1998). The land surface reflectance parameters currently being generated at the NASA Langley Atmospheric Sciences Data Center (ASDC) include the spectral hemispherical–directional reflectance factors (HDRF) at the nine MISR view angles and the associated bihemispherical reflectances (BHR). The hemispherical directional reflectance factor (HDRF) and the bihemispherical reflectance (BHR) characterize the surface reflectance under ambient sky conditions, i.e., direct and diffuse illumination. The bidirectional reflectance factor (BRF) and the directional hemispherical reflectance (DHR) are defined for the unique case when the atmosphere is absent, that is black sky

conditions. An algorithm for the generation of vegetation green leaf area index (LAI) and the fraction of photosynthetically active radiation absorbed by vegetation (FPAR) from MISR BHR and BRF was implemented for operational processing in October 2002 (Knyazikhin, Martonchik, Diner et al., 1998). An additional goal of the MISR LAI/FPAR algorithm is the classification of global vegetation into biome types; a parameter that is usually specified as an input in certain algorithms that use single-angle observations for the retrieval of surface properties (Myneni et al., 2002). In this paper, we describe performance of the implemented version of the MISR LAI/FPAR algorithm with retrievals from Africa as a test case.

The quality and spatial coverage of BHR and BRF determine the quality and spatial coverage of the LAI and FPAR products. Therefore, we start with a description of the MISR data and analyses of uncertainties in MISR surface reflectances, followed by a discussion of the spatial scaling issues associated with the MISR LAI/FPAR algorithm. At this initial stage, analyses that assess performance of the algorithm as a function of uncertainties in the MISR BHR and BRF data and the development of retrieval quality indicator flags are emphasized.

2. MISR data

The MISR data distributed from the NASA Langley Atmospheric Sciences Data Center were used in this study. The MISR data are in the format of path (swath) and orbit. The entire earth surface is covered in 233 paths; each path is about 360 km wide from East to West. Each orbit corresponds to data acquired over a path for a particular date. Each path is divided into 180 blocks measuring 563.2 km (cross-track) × 140.8 km (along-track), that is 512 × 128 pixels. For a given path, a numbered block always contains the same geographic locations.

The MISR Level 2 Surface Parameters Product contains information on land surface directional reflectance properties, albedos (both spectral and PAR integrated) and associ-

ated radiation parameters. These data, in HDF format and at 1.1-km spatial resolution, are the source of BRFs, HDRFs, DHRs, and BHRs (expansion of all abbreviations is given in a list at the beginning of this article).

The view angles at the surface for each of the nine MISR cameras, as well as the incident solar angle at the surface, are contained in the MISR Geometric Parameters Product. This information is at a spatial resolution of 17.6 km and is input to the LAI/FPAR algorithm. The latitude and longitude information is contained in the MISR Ancillary Geographic Product (MISR Data Products Specifications Document).

A look-up table (LUT) approach is used to rapidly model the radiative transfer process of complex canopy/soil models to determine the matching modeled reflectances and the associated values of LAI and FPAR. For efficiency in execution of the algorithm, all necessary radiative transfer parameters have been precomputed and stored in the Canopy Architecture Radiative Transfer (CART) file.

MISR data (version v2.2_i4) from Africa covering the vegetated surface between 19.02°N and 35.34°S were selected for this investigation as in situ LAI and FPAR measurements were available from several sites in southern Africa (Tian et al., 2002a,b). These field data, although collected in 2000, are useful for estimating certain algorithm parameters, as detailed elsewhere in this article. In particular, the analysis is focused on southern Africa with MISR data from March 2001—the earliest period for which the MISR LAI/FPAR products are available.

MISR has a ground track repeat cycle every 16 days and achieves global coverage every 9 days. However, in view of cloud cover, data from an entire month are required to obtain full coverage of southern Africa. Assembling the data set in this fashion meant an implicit assumption that vegetation changes were minimal in this one month composite period, introducing uncertainty into the derived results. This uncertainty will be assessed during the course of this investigation.

The moderate spatial resolution, multi-spectral, and multi-angle aspects of the MISR instrument imply large
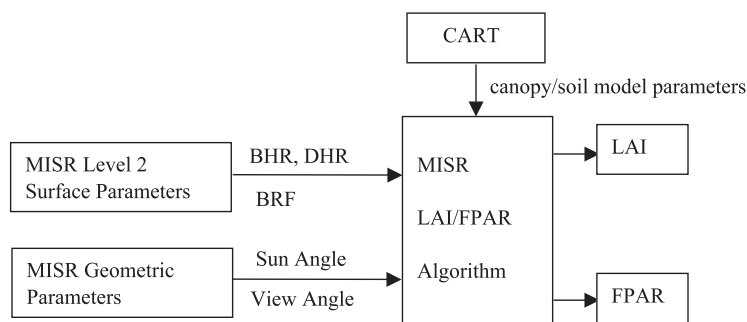

Fig. 1. Flow chart of the relationship between MISR LAI/FPAR algorithm and data. The inputs, BHR, DHR, and BRF are from the MISR Level 2 Surface Parameters Product, the sun and view angles from the MISR Geometric Parameters Product, and canopy/soil model parameters from the CART file.

data volumes and hence the need for analysis stratified by biome type. Raw data that were corrupted or with missing geometry information (flagged with fill values) were excluded from the analysis. Likewise, invalid reflectance data, for example, BHRs greater than 1, were ignored. A schematic chart of the data processing is shown in Fig. 1. The ratio of pixels with valid data to the total number of vegetated pixels from paths 162 to 203 is shown in Fig. 2, separately for different biomes. The data from each path are from different days in March 2001. About 46% of the pixels contain valid data, useful as inputs to the algorithm. This number changes by date and by biome type, and may be as low as 31.5% in the case of tropical humid forests, where cloud cover is persistent.

3. Data analysis

The nominal view angles for the nine cameras are $0.0°$, $\pm 26.1°$, $\pm 45.6°$, $\pm 60.0°$, and $\pm 70.5°$. The variations in actual view angles relative to the specification, for the fore and aft off-nadir sensors, are shown in Fig. 3. The maximum deviation in view zenith angles is for camera A fore and aft ($4.95°$ and $4.84°$, respectively). These deviations decrease with increasing view zenith angle. Most of the deviations are positive. This is a geometric effect. The MISR data are in the Space Oblique Mercator (SOM) projection, in which the reference meridian nominally follows the spacecraft ground track. It maps the earth latitude and longitude to a SOM coordinate system that is approximately fit into MISR
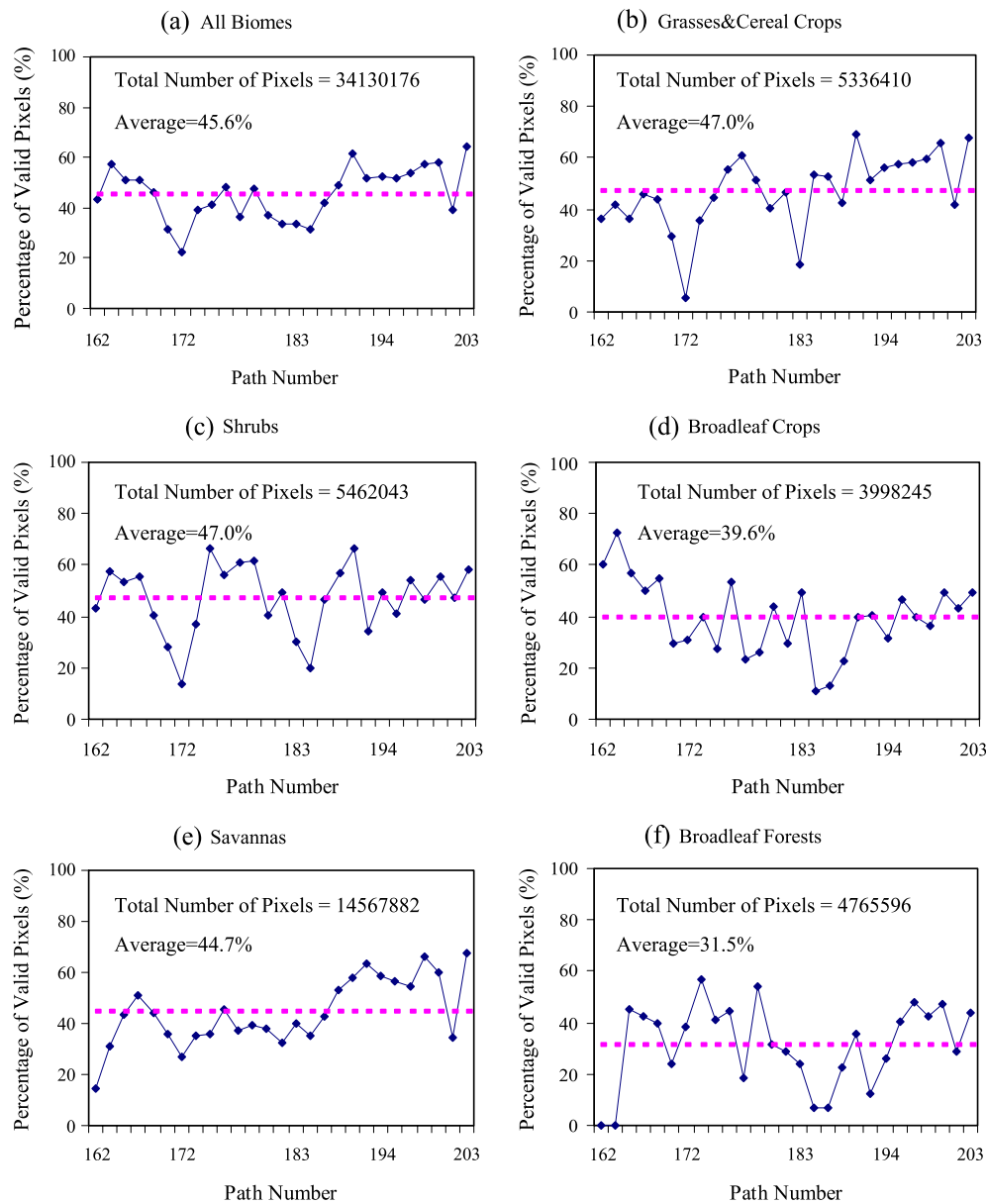

Fig. 2. Ratio of valid pixel number to total pixel number, in percentage. (a) All biomes, (b) grasses and cereal crops, (c) shrubs, (d) broadleaf crops, (e) savannas, and (f) broadleaf forests. There is no significant presence of needleleaf forests in Africa. The average ratio is shown in these plots as a dashed line. The maximum percentage of valid pixels is for shrubs (47%) and the minimum is 31.5% for broadleaf forests.
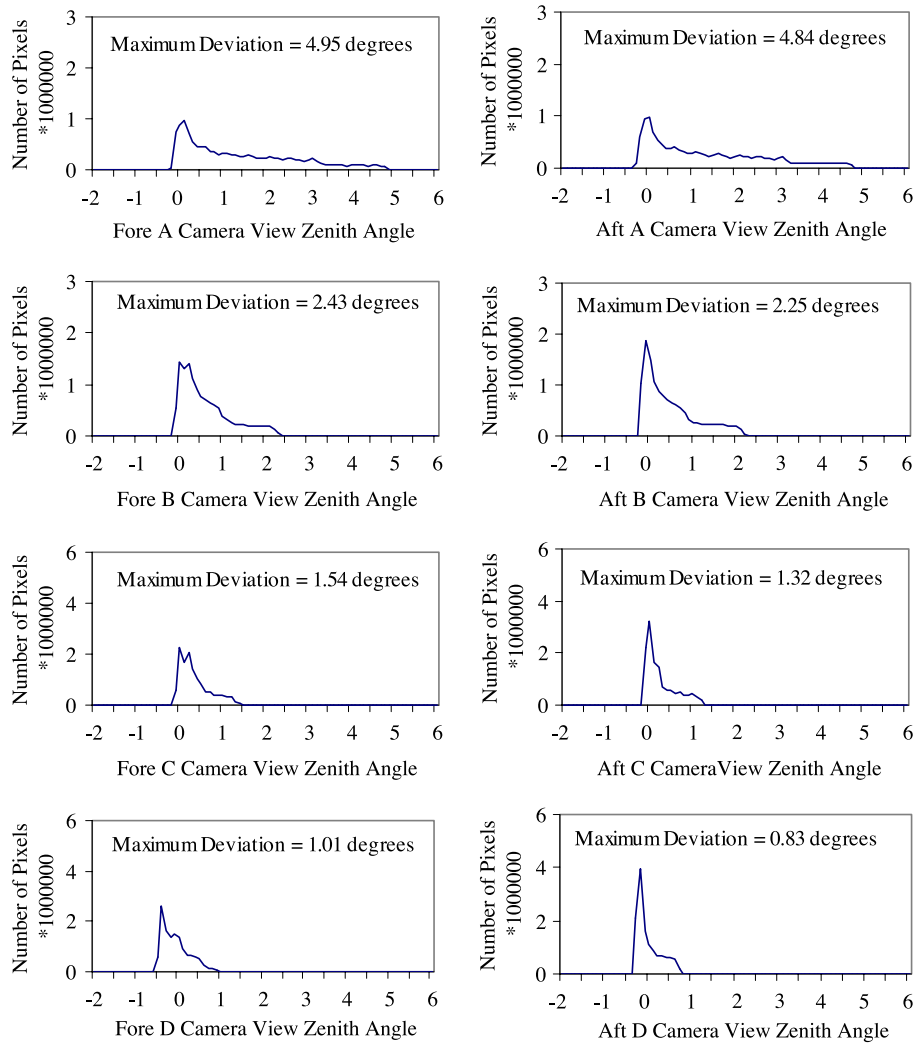
Fig. 3. Histograms of the difference between nominal and actual viewing angles. The maximum deviation is given for each camera.

swath. The center of the block has the nominal view angles; since a block is 563 km wide, the view angle increases from the center to the edge of the block. The effect is most pronounced in the nadir camera, where the view angle is 0° at the center and 18° at the edge of the block. This problem can be avoided if one uses data from the center of the swath only. Even with the variations they still fall within the view angle bin limits in the CART file.

Uncertainties in land surface reflectances determine the quality of retrieved LAI and FPAR values (Wang et al., 2001). The calibration and processing for atmospheric effects of the measured radiances induce uncertainties in surface reflectances. Land surface reflectance parameters, such as BRF and BHR, are inputs of the LAI/FPAR algorithm. Therefore, the uncertainties in MISR surface reflectance product are evaluated below, using two different methods, spatial and temporal.

MISR surface reflectance data were first sorted according to the biome type. The at-launch Moderate Resolution Imaging Spectroradiometer (MODIS) biome map was used to identify the pixel biome type (Lotsch, Tian, Friedl, & Myneni, 2003). This map segregates global vegetation into six major biome types depending on vegetation structure and optical properties, and background characteristics (Myneni, Nemani, & Running, 1997). The six biomes include: grasses and cereal crops (biome 1), shrubs (biome 2), broadleaf crops (biome 3), savannas (biome 4), broadleaf forests (biome 5), and needleleaf forests (biome 6). The site-based accuracy of this map is 73% (Lotsch et al., 2003). The kappa coefficient (κ) (Cohen, 1960), which provides a correction for the proportion of chance agreement between reference and test data, is 0.68 (Lotsch et al., 2003). When compared to maps generated from the same data but classified using the International Geosphere Biosphere Program (IGBP) classes (Hansen, Defries, Townshend, & Sohlberg, 2000; Loveland et al., 1995), the biomes were mapped with ~ 5% higher overall accuracy (Lotsch et al., 2003). It should be noted that this classification accuracy analysis is based on sites that are a priori pure and therefore will not include errors due to sub-pixel mixing. The upper-

left and bottom-right latitude and longitude of the MISR data block were used as georeferences to reproject the at-launch MODIS biome map to the MISR SOM projection. Data density distribution functions, defined as the number of pixels per unit area in the red-NIR space, were evaluated for each biome type. Pixels located around the data peak, i.e. the maximum pixel number, can be interpreted as the set of pixels representing the most probable pattern of canopy structure. As an example, the data density distribution function for Broadleaf Forests is shown in Fig. 4a. Such pixels were selected for further analysis.

The mean and standard deviation of the HDRFs and BHRs evaluated from pixels about the data peak (the spatial method) are shown in Fig. 4b–d, for different biomes. Uncertainties in HDRFs are larger at large view angles (except the A fore and Aft cameras), and greater in the near-infrared channel than the red channel, with one excep-

tion (standard deviations in the red channel for the nine view angles, from angle 1 to angle 9 are 0.031, 0.019, 0.015, 0.016, 0.016, 0.014, 0.013, 0.019, 0.042; standard deviations in the NIR channel for the nine view angles are 0.033, 0.026, 0.024, 0.023, 0.024, 0.019, 0.017, 0.022, 0.040). The uncertainties are generally similar in the fore and aft angles. The BHR magnitudes with respect to biome type, shown in Fig. 4d, display expected behavior. In the red channel, shrubs are brighter and the BHR magnitude decreases with increased tree cover. In the near-infrared, the opposite is seen. Although the uncertainties are generally comparable at both wavelengths, they are considerably larger in the red channel on a relative basis.

The uncertainties in Fig. 4b–d may result from variations in view angles, sun angles, variation in vegetation canopy structure and atmospheric correction. Deviations from nominal view zenith angles were small (Fig. 3). The angular
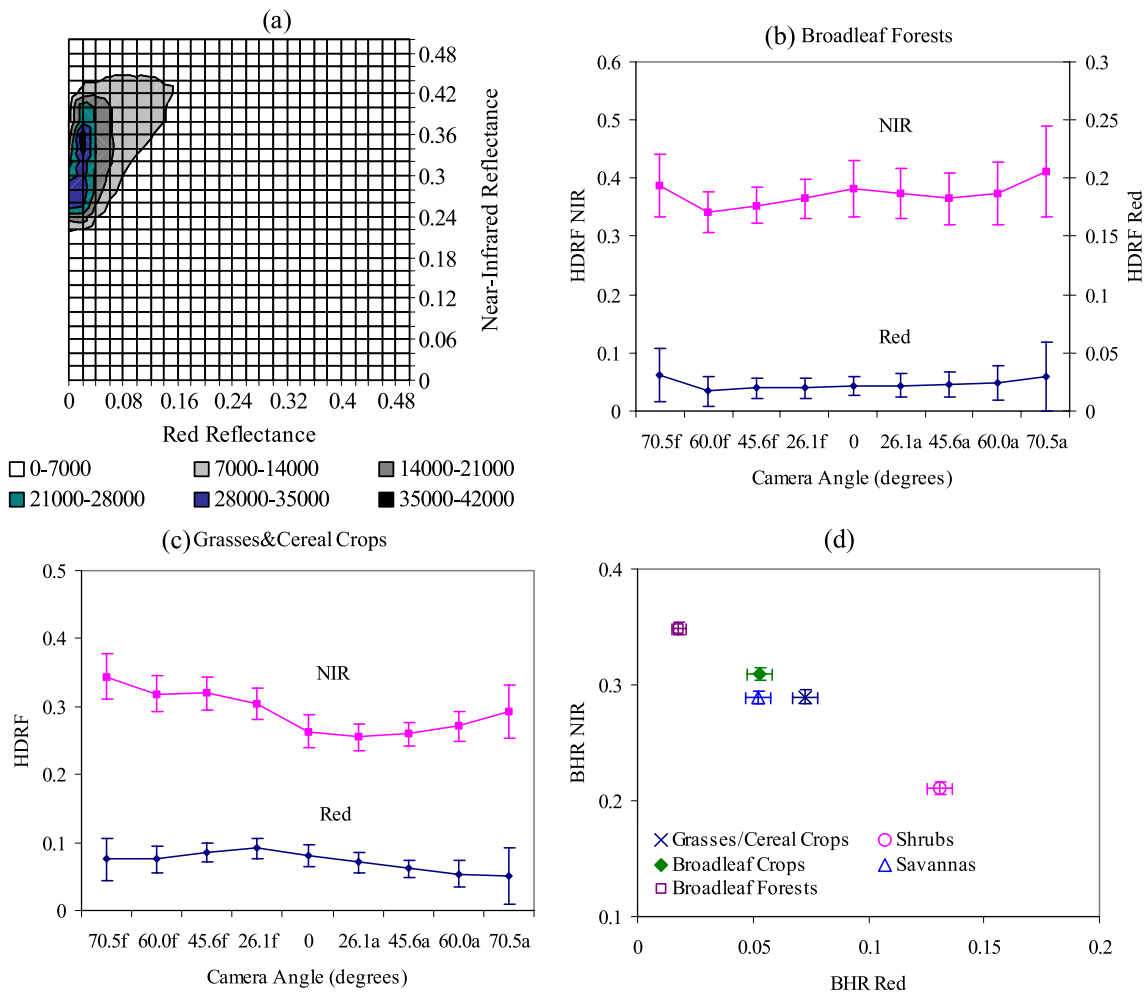

Fig. 4. (a) Distribution of pixel counts in the red and near-infrared DHR space for broadleaf forests. Pixels located around data peak (0.02, 0.36) may be interpreted as pixels characteristic of broadleaf forests. (b) The mean and standard deviation of HDRFs in the perpendicular plane at red and NIR wavelengths derived from pixels around the data peak for broadleaf forests. The solar zenith angle and azimuth are $23 \pm 2°$ and $288 \pm 9°$, respectively. (c) The mean and standard deviation of HDRFs at red and NIR wavelengths derived from pixels around the data peak for grasses and cereal crops. The solar zenith angle and azimuth are $32 \pm 3°$ and $232 \pm 5°$, respectively. Values of the difference between solar and view azimuth are $217 \pm 10°$ for forward cameras and $37 \pm 10°$ for afterward cameras. (d) Mean and standard deviation of MISR BHR values from pixels near the data peak (there is no appreciable needleleaf forests presence in Africa).

signature of broadleaf forests, which is in the 90° azimuth plane relative to sun is shown in Fig. 4b. The solar zenith angle and azimuth are $23 \pm 2°$ and $288 \pm 9°$, respectively. For grasses and cereal crops (Fig. 4c), the solar zenith angle is $32 \pm 3°$ and solar azimuth is $232 \pm 5°$. Values of the difference between solar and view azimuth are $217 \pm 10°$ for forward cameras and $37 \pm 10°$ for afterward cameras. Variations due to sun-view geometry differences, therefore, are small. Vegetation cover type mixture may also contribute to uncertainties in reflectance data. Variations in canopy structure due to biome mixtures are minimized by selecting pixels around the data peak. These pixels may be considered representative of a biome type with minimal mixing. Therefore, uncertainties due to biome mixture are unlikely to be the cause of variations seen in Fig. 4b–d.

Thus, uncertainties in BHR and HDF remain even after accounting for minor uncertainties due to variations in view angles and cover type. The residual uncertainties may be due to atmospheric correction, and this is further investigated in the following temporal analysis.

In this method, we assume the vegetation structure to remain unchanged during the month of March. The coefficients of variation (standard deviation divided by the mean) of the MISR BHR in blue, red, and NIR bands from 3 different days from path 178 are shown in Fig. 5 for different biomes. The histograms are wide, especially in the blue band for both grasses and cereal crops and broadleaf forests, which is likely due to correction for atmospheric effects. Likewise, the histograms are broad at the red band, especially in the case of broadleaf forests. The most probable value of the coefficient of variation is least for the NIR band (about 0.15 for grasses and cereal crops and about 0.4 for broadleaf forests).

Data from only three different days in March were available for this analysis and this sample is clearly insufficient. These uncertainties are considered as very rough

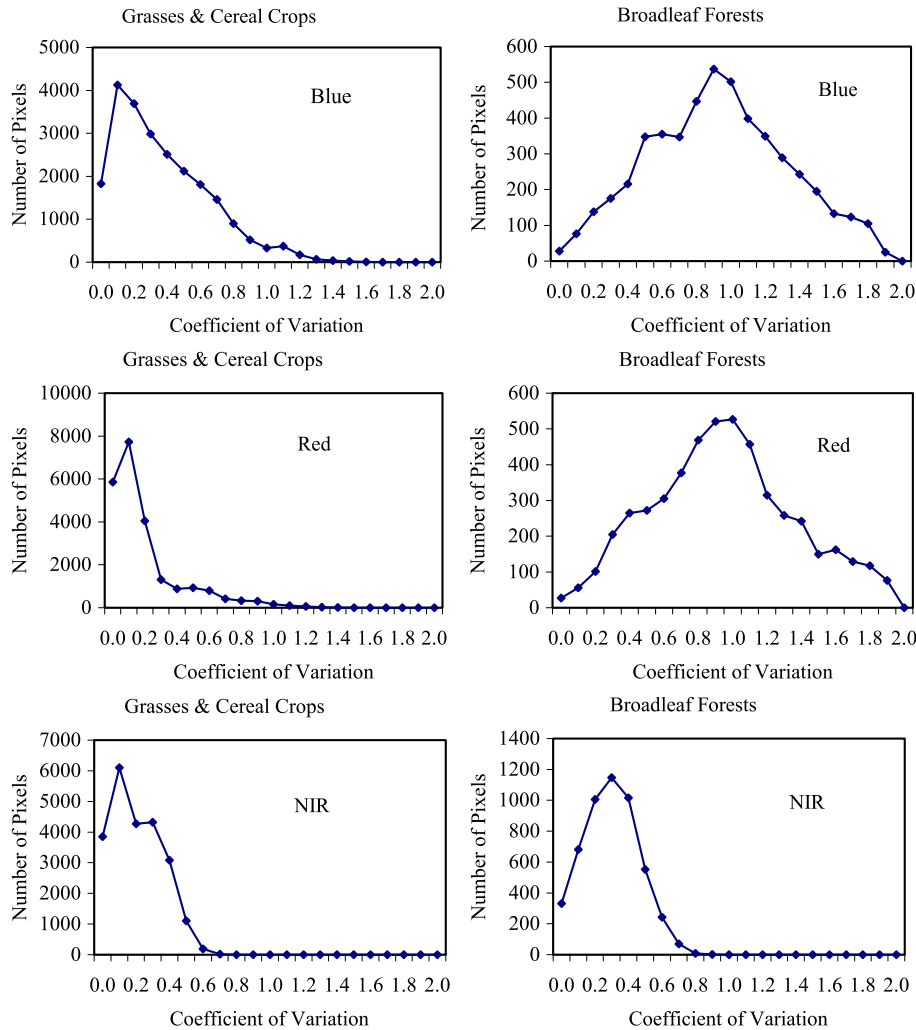Fig. 5. Histograms of the coefficient of variation (standard deviation/mean) of the MISR BHR from path 178 for 3 different days, orbit 6393 (Mar. 1, 2001), 6626 (Mar. 17, 2001), and orbit 6859 (April 2, 2001). Coefficients of variation of the solar zenith angle and azimuth do not exceed 0.07 for data used. The plots are for grasses and cereal crops and broadleaf forests at blue, red and NIR bands.
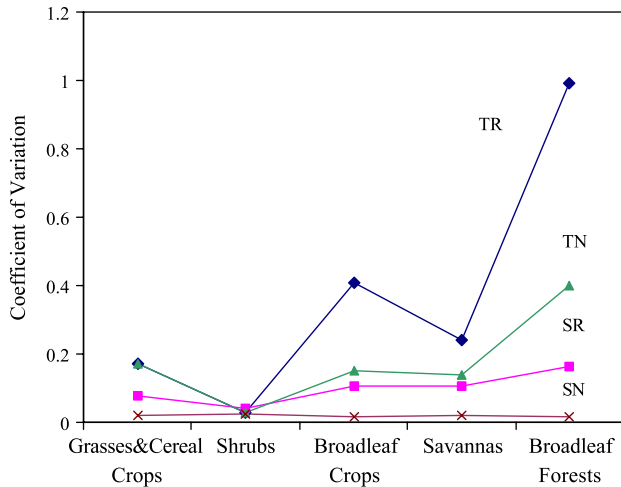
Fig. 6. Mean coefficient of variation of DHR at red and NIR wavelengths derived from spatial and temporal analyses of MISR data. The data described in Figs. 4d and 5 were used to derive spatial and temporal variation in MISR surface reflectance. Labels TN and TR refer to the temporal, and SR and SN refer to the spatial coefficients of variation at red and NIR spectral bands.

estimates of the upper bounds of uncertainties in the MISR surface reflectances. At least in the case of broadleaf forests, the LAI does not change much during the peak green season. Therefore, variations in canopy structure can be excluded for this cover type. Coefficients of variation of solar zenith angle and azimuth did not exceed 0.07 for data shown in Fig. 5 and thus the impact of the sun angular geometry on variation in the MISR BHR is negligible. The large uncertainties here may be due to errors in pixel geolocation, or may be due to atmospheric correction.

From the comparison presented in Fig. 6 between uncertainties estimated from spatial (Fig. 4) and temporal (Fig. 5) analyses, it is obvious that uncertainties from the temporal analysis are greater than the uncertainties from spatial analysis for most biome types, with the exception of shrubs, where both kinds of uncertainties are similar in both bands. The uncertainties of the temporal analysis are significant and they are taken as the upper bounds in the LAI/FPAR retrievals discussed in this article.

4. MISR LAI/FPAR algorithm

The MISR algorithm retrieves LAI and FPAR values using a two-step process. The first step involves a comparison of the MISR BHR with those determined from a suite of canopy models, which depend on biome type, canopy structure, and soil/understory reflectances. All canopy, soil, and biome patterns for which the modeled and observed BHRs in the four spectral bands differ by an amount equivalent to or less than the uncertainty in model and observations are considered as acceptable solutions. FPAR is calculated for each acceptable solution. For each biome pattern bio, bio = 1, 2, ..., 6, the algorithm then

evaluates mean $LAI_1(bio)$ and $FPAR_1(bio)$ over acceptable solutions, their dispersions, $\Delta LAI_1(bio)$, $\Delta FPAR_1(bio)$, and number $N_{sol,1}(bio)$ of acceptable solution. Eq. (2) with overall uncertainties in modeled and observed BHRs is used to execute the first step. The biome, canopy, and soil patterns that pass this comparison test are subject to the second step, which is comparison of directional signatures of modeled and observed BRFs. Again, for each biome type, mean $LAI_2(bio)$ over acceptable solutions, its dispersion, $\Delta LAI_2(bio)$ and number $N_{sol,2}(bio)$ of acceptable solutions are evaluated. Eq. (3) with appropriate overall uncertainties is used to execute the second test. For each 1.1-km MISR pixel within which the BHR/BRF retrieval was performed, $LAI_1(bio)$, $\Delta LAI_1(bio)$, $N_{sol,1}(bio)$, $LAI_2(bio)$, $\Delta LAI_2(bio)$, and $N_{sol,2}(bio)$, bio = 1, 2, ..., 6, are archived in the MISR Aerosol/Surface Product. The FPAR is evaluated and archived for each 17.6-km region.

An additional goal of the MISR LAI/FPAR algorithm is the classification of vegetation in terms of biome types described in the previous section, a parameter that is usually specified as an input to other algorithms that use single-angle observations. Based on the output archived, the following biome identification algorithm will be examined here. Assuming that more than one of the candidate biomes passes the second test (the comparison of retrieved and modeled directional reflectances), the biome type with the minimum coefficient of variation ($\Delta LAI_2/LAI_2$) of LAI (COVLAI) is chosen as being most representative of the observed vegetation type for that pixel. If the same minimum COVLAI is found for more than one biome type, then the biome type with the smallest mean LAI is chosen. If this process fails to identify a unique biome type, the retrieval is classified as unsuccessful.

5. Scaling of the algorithm

In the MISR LAI/FPAR algorithm, the three-dimensional radiative transfer equation is used to simulate canopy reflectances as a function of biome type, sun-view geometry, and canopy/soil patterns (Knyazikhin et al., 1998). Global vegetation is stratified into six canopy architectural types or biomes mentioned earlier. The structural attributes of these biomes are parameterized in terms of variables that the radiative transfer equation admits (Myneni et al., 1997). The radiative transfer equation was adjusted to model canopy reflectances of the six biome types at 30 m spatial resolution, which is taken as the reference resolution. However, when the spatial resolution of the imagery becomes significantly coarser than 30 m, both the degree of biome mixing within a pixel and the number of mixed pixels in the imagery increase. LAI retrieval errors increase as biome mixing in pixels increases if the within-pixel heterogeneity is not accounted for (Tian et al., 2002a,b). Errors for the pixels in which forests are minority biomes in non-forest pixels are particularly larger than pixels within

which forest biomes are mixed with one another. Thus, the retrieval algorithm must be scale-adjustable, to allow for spatial scale effects. Here, we follow a technique developed by Tian et al. (2001), which accounts for pixel heterogeneity by modifications to the single scattering albedo that the radiative transfer equation admits through the use of land cover fractions.

To specify appropriate values for the single scattering albedo, the MISR DHRs corresponding to the peak green season are located in the red-NIR spectral space for each of the biome types (Fig. 4a). Pixels located around the data peak can be interpreted as the set of pixels representing the most probable pattern of canopy structure. Neglecting contribution of the surface underneath the canopy, the most probable value of DHR at wavelength λ is related to canopy transmittance and absorptance at this wavelength as (Knyazikhin et al., 1998; Panferov et al., 2001; Shabanov et al., in press; Zhang, Shabanov, Knyazikhin, & Myneni, 2002)

$$1 - \mathrm{DHR}_\lambda = \frac{q}{1 - \omega_\lambda p_t} + \frac{1 - \omega_\lambda}{1 - \omega_\lambda p_i}(1 - q). \quad (1)$$

Here ω_λ is the single scattering albedo defined as the ratio of energy scattered by the elementary volume formulated for the radiative transfer equation, to energy intercepted by this volume; q is the probability that a photon in the incident radiation will arrive at the bottom of the canopy without suffering a collision (uncollided radiation), $\omega_\lambda p_t$ and $\omega_\lambda p_i$ are portions of collided radiation in total radiation transmitted and intercepted by the vegetation canopy, respectively (Shabanov et al., in press; Wang et al., in press). The wavelength independent parameters q, p_t, and p_i are functions of LAI. Eq. (1) expresses the energy conservation law, namely, the radiation absorbed by a vegetated surface (the left-hand side) is the sum of radiant energy absorbed by the underlying surface and vegetation (the first and second terms on the right-hand side of Eq. (1), which are the canopy transmittance, $t_{bs,\lambda}$, and absorption calculated for the case of a black surface underneath the canopy). In the case of a reflecting Lambertian surface, the term $(\rho_\lambda/(1 - \rho_\lambda r_{s,\lambda}))t_{s,\lambda}t_{bs,\lambda}$ should be subtracted from the left-hand side of Eq. (1) to account for the contribution of the ground to the canopy leaving radiation (see Eq. (41) in Knyazikhin et al., 1998). Here, ρ_λ is the reflectance of the underlying surface; $t_{s,\lambda}$ and $r_{s,\lambda}$ are frac-

tions of radiation transmitted and reflected by the vegetation canopy if it were illuminated from below by an isotropic source (Knyazikhin et al., 1998).

Leaf area index values corresponding to the most probable canopy realization must be known in order to calibrate
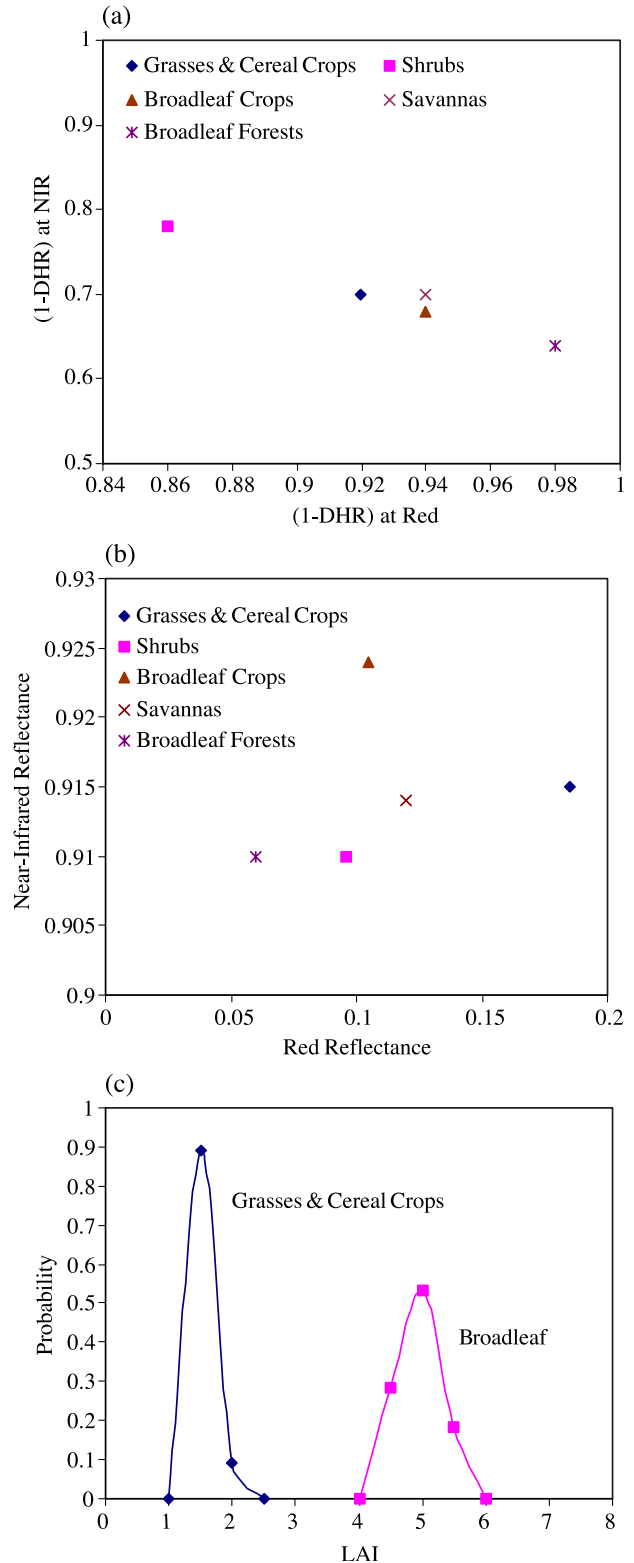

Fig. 7. (a) Fraction of energy (1-DHR) absorbed by the vegetated surface at red and NIR wavelengths by different cover types. Pixels located around the data peak (see Fig. 4a) were used to derive values of (1-DHR). (b) Adjusted single scattering albedos of different cover types used by the operational MISR LAI/FPAR software. (c) Histogram of LAI values produced by the MISR algorithm using surface reflectances located around the data peak (see Fig. 4a). Single scattering albedos shown in (b) were used. Uncertainties in MISR BHRs and BRFs were set to 0.2 based on analysis presented in Figs. 4–6. The left curve is for grasses and cereal crops with peak probability at LAI = 1.5 (mean LAI = 1.27) and the right curve is for broadleaf forests with peak probability at LAI = 5.0.

the algorithm, and this is usually accomplished through field measurements. Given biome type and LAI, as well as measured DHR_λ, and modeled q, p_t, and p_i corresponding to this LAI value, the algorithm is then adjusted for data resolution by finding values of the single scattering albedo ω_λ, which provide the best agreement between the left and right sides of Eq. (1). Values of DHR for Africa, obtained from MISR retrievals (1–23 March 2001) and field measurements made during the SAFARI 2000 wet season campaign (3–18 March 2000) and the Operation Canopy La Makande'99 campaign (2–10 March 1999) (Panferov et al., 2001), were used to scale the LAI/FPAR algorithm to the MISR resolution. The MODIS biome classification map was used to sort the MISR DHR data into individual biome classes. The spectral ground reflectance ρ_λ is assumed to vary within given biome-dependent ranges representative of reflective properties of the most probable surfaces underneath the canopy (Knyazikhin et al., 1998).

The above method was followed to scale the MISR LAI/FPAR algorithm. The most probable data, which have minimal variations in vegetation structure, are used as the input data. Fig. 7a shows locations of the most probable values of $(1 - DHR_\lambda)$ at red and NIR wavelengths, for different biomes. The algorithm is adjusted for data resolution by finding values of the single scattering albedo, which provide the best agreement between the retrieved and measured LAI values. The solutions to this problem are shown in Fig. 7b. These single scattering albedos are used by the operational MISR LAI/FPAR software. Fig. 7c shows histograms of LAI retrievals for grasses and cereal crops and broadleaf forests, which are centered at about 1.5 and 5.0, respectively. These mean values agree well with LAI measured in the field (Myneni et al., 2002; Privette et al., 2002).

6. Performance of the algorithm as a function of uncertainties

At least two types of uncertainties influence the quality of LAI/FPAR retrievals-uncertainties in measured and modeled land surface reflectances. In general, these uncertainties set a limit to retrieval quality; that is, the retrieval accuracy cannot be better than summary accuracy in input data and the model. If uncertainties are ignored, it can result not only in the loss of information conveyed to the algorithm, but also in its destabilization (Wang et al., 2001). Thus, the use of uncertainty information in the retrieval technique can influence the quality of retrievals. An overall uncertainty in model and measurements is input to the MISR LAI/FPAR algorithm (Knyazikhin et al., 1998). Our aim here is to evaluate an upper limit of acceptable uncertainties in data and observations which allow the algorithm to discriminate between pure biome types, to minimize the impact of biome misidentification on LAI retrievals, and to maximize the number of successful retrievals.

6.1. Definition of uncertainties

Let A_k and $r_{k,i}$, $k = 1, 2, \ldots, 4$, $i = 1, 2, \ldots, 9$, be atmospherically corrected BHRs at four spectral bands and BRFs at four spectral bands and in nine MISR directions, respectively. We treat these values as independent random variables with finite variances $\sigma_A(k)^2$ and $\sigma_r(k,i)^2$, $k = 1, 2, \ldots, 4$, $i = 1, 2, \ldots, 9$, and assume that the deviations $\varepsilon_k = (A_k - \bar{A}_k)/\sigma_A(k)$ and $\delta_{k,i} = (r_{k,i} - \bar{r}_{k,i})/\sigma_r(k,i)$ follow Gaussian distributions. Here $\bar{A}_k$ and $\bar{r}_{k,i}$, are the mathematical expectations of A_k and $r_{k,i}$, which are treated as "true values." The random variables,

$$\chi_A^2 = \sum_{k=1}^{N_{bands}} \varepsilon_k^2 = \sum_{k=1}^{N_{bands}} \frac{(A_k - \bar{A}_k)^2}{\sigma_A(k)^2}, \tag{2}$$

$$\chi_r^2 = \sum_{i=1}^{N_{view}} \sum_{k=1}^{N_{bands}} \delta_{k,i}^2 = \sum_{i=1}^{N_{view}} \sum_{k=1}^{N_{bands}} \frac{(r_{k,i} - \bar{r}_{k,i})^2}{\sigma_r(k,i)^2}, \tag{3}$$

characterizing the proximity of atmospherically corrected data to true values have chi-square distributions. Here, N_{bands} and N_{view} are the number of spectral bands and view directions for which MISR observations are available. Inequalities $\chi_A^2 \le N_{bands}$ and $\chi_r^2 \le N_{bands} N_{view}$ indicate good accuracy in the atmospherically corrected surface reflectances with a high probability. Dispersions $\sigma_A(k)$ and $\sigma_r(k,i)$ are uncertainties in the land surface reflectance product, which are input to the MISR LAI/FPAR algorithm. Model uncertainties, $\sigma_{A,m}(k)$ and $\sigma_{r,m}(k,i)$ can be defined in a similar manner (Wang et al., 2001). Note that currently the MISR algorithm uses two spectral bands, red, and NIR ($N_{bands} = 2$) to retrieve the pixel LAI and FPAR values.

Overall uncertainties in BHR, $\delta_A(k)$, and BRF, $\delta_r(k,i)$, which guarantee the convergence property of the retrieval technique (i.e., increasingly accurate retrievals with increasingly accurate inputs) can be represented as $\delta_A(k)^2 = [\sigma_A(k)^2 + \sigma_{A,m}(k)^2]/\theta_A^2$, $\delta_r(k,i)^2 = [\sigma(k,i)^2 + \sigma_{r,m}(k,i)^2]/\theta_r^2$. Here, the stabilization parameters θ_A and θ_r vary between 0.5 and 1 (Wang et al., 2001). To evaluate proximity of observed to modeled surface reflectances, true values $\bar{A}_k$, $\bar{r}_{ki}$, and uncertainties in the surface reflectance product $\sigma_A(k)$ and $\sigma_r(k,i)$ that appear in Eqs. (2) and (3) should be substituted with modeled reflectances and overall uncertainties (Wang et al., 2001). We assume that the model uncertainties do not exceed uncertainties in observations, that is $\sigma_{A,m}(k)/\sigma_A(k) < 1$ and $\sigma_{r,m}(k,i)/\sigma(k,i) < 1$. The overall uncertainties in BHR and BRF can be represented as $\delta_A(k) = (\alpha_A/\theta_A)\sigma_A(k)$ and $\delta_r(k,i) = (\alpha_r/\theta_r)\sigma_r(k,i)$, respectively. Here, the coefficients α_A and α_r vary between 1 and 2. A correct specification of the ratios $\gamma_A = (\alpha_A/\theta_A)$ and $\gamma_r = (\alpha_r/\theta_r)$, each varying between 1 and 4, are required to achieve an optimal performance of the algorithm (Wang et al., 2001). Inequalities $\chi_A^2 \le N_{bands}$ and $\chi_r^2 \le N_{bands} N_{view}$ with appropriate overall uncertainties are

used to execute the first and second comparison tests (Section 4).

6.2. Optimal performance of the algorithm

The analysis presented earlier showed that uncertainties in surface reflectances can be quite high (Figs. 4 and 5). Fig. 2 shows the availability of valid MISR surface reflectances, which, on average, constitute 42% of the vegetated land for

the selected paths. A subset of these surface reflectances whose uncertainties exceed a certain acceptable level will result in algorithm failure, reducing the number of successful LAI and FPAR retrievals. This number can be increased by setting the ratios γ_A and γ_r to higher values. The retrieval quality, however, will decrease in this case. A decrease in γ_A and γ_r will result in fewer successful retrievals. It should be emphasized that this does not necessarily improve the retrieval quality. In general, the underestimation of the overall
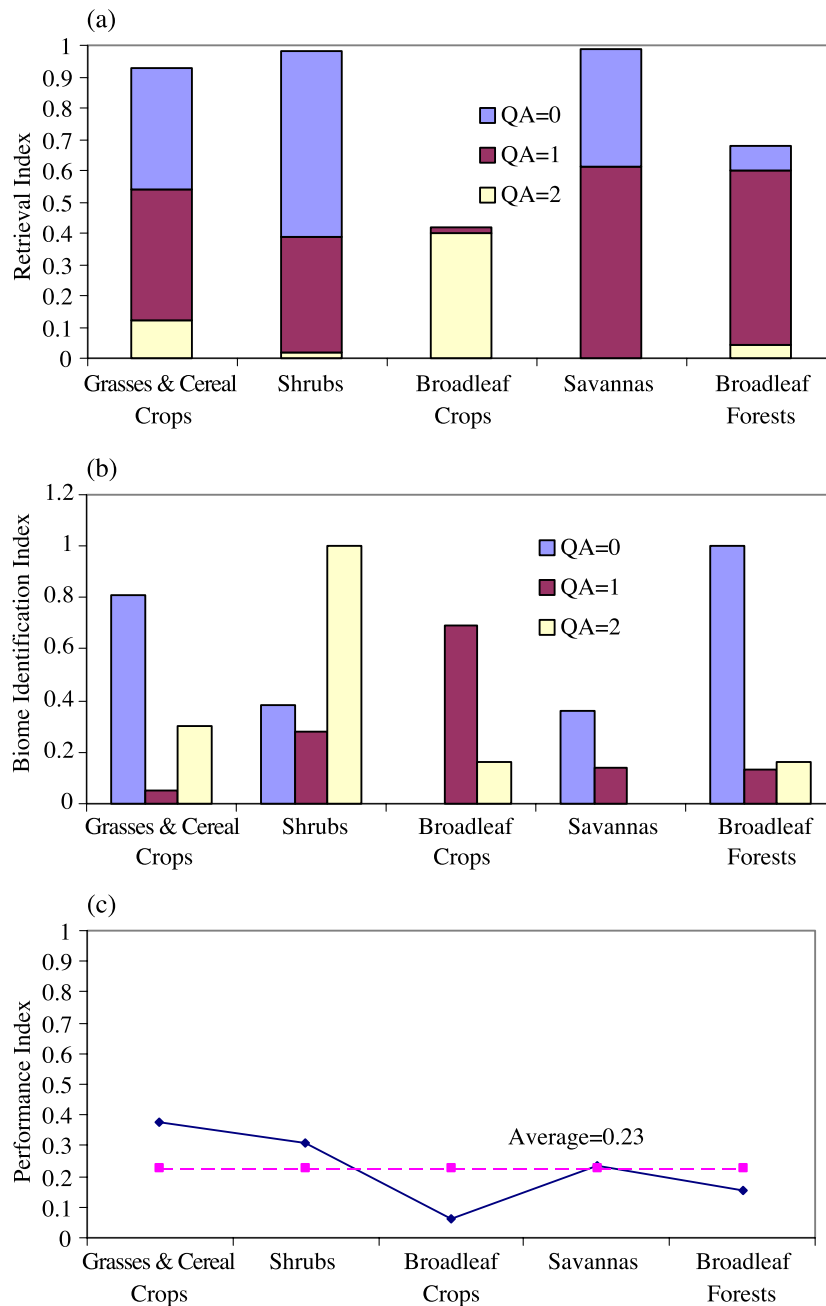
Fig. 8. (a) Retrieval index as a function of biome type and QA for optimal set of relative uncertainties listed in Tables 1 and 2. Pixels located around the data peak and the six-biome map were used to derive values of the retrieval index. In this case, the retrieval index is the conditional probability of retrieving LAI value given the biome type. (b) BI as a function of biome type and QA for the optimal set of relative uncertainties. Pixels for which the MISR algorithm retrieved LAI values using the six-biome map and surface reflectance located around data peaks were used to evaluate the BI. (c) PI as a function of biome type for the optimal set of relative uncertainties.

Table 1
Optimal values of relative uncertainties, v_A, in modeled and observed BHRs

Biome type	Grass and cereal crops	Shrubs	Broadleaf crops	Savanna	Broadleaf forests
Red	0.2	0.08	0.15	0.4	0.2
NIR	0.05	0.05	0.05	0.1	0.2

uncertainties can result in lower retrieval quality than their overestimation (Wang, 2001). Our aim here is to evaluate optimal values of γ_A and γ_r, which allow the algorithm to discriminate between pure biome types, to minimize the impact of biome misidentification on LAI retrievals, and to maximize the number of successful retrievals.

Two variables are used to characterize the algorithm performance as a function of uncertainties. The first is the retrieval index (RI), defined as the ratio of the number of retrieved LAI values to the total number of pixels with valid surface reflectance data. This variable does not characterize retrieval quality, but shows the spatial coverage of the retrieved LAI and FPAR fields. In other words, $(1 - \mathrm{RI})$ is the probability that the algorithm will fail to retrieve LAI and FPAR and, as a result, return a fill value. The second is the biome identification index (BI), the ratio of the number of cases for which the algorithm correctly identifies the biome type to the number of successfully retrieved pixels. The at-launch MODIS biome map (Section 3) was used as the reference biome classification map.

The following procedure was executed to specify optimal values of the overall uncertainties. For each biome type, pixels located around the data peak were selected (Fig. 4a). Given values of the ratios γ_A and γ_r for each biome type, the MISR LAI/FPAR algorithm was executed using these surface reflectances and the six-biome map described earlier. From the initial set, pixels that pass the first and/or second tests are selected. A quality assessment (QA) flag is assigned to each pixel, indicating that a retrieval resulted from both tests (QA = 0, highest quality), the first test only (QA = 1, intermediate quality), or the second test only (QA = 2, low quality). The RI as a function of QA and biome type is also calculated. The biome identification algorithm is then applied and the BI as a function of QA is calculated. In this procedure, the RI is the conditional probability of retrieving a LAI value given biome type, while the BI is the probability of identifying the biome type. By calculating RI(γ_A, γ_r, bio, QA) and BI(γ_A, γ_r, bio, QA) for all possible combinations of the ratios γ_A and γ_r, we select those that result in the maximum of the performance index (PI),

$$\mathrm{PI(bio)} = \sum_{\mathrm{QA}=0}^{2} \mathrm{RI}(\gamma_A, \gamma_r, \mathrm{bio}, \mathrm{QA}) \cdot \mathrm{BI}(\gamma_A, \gamma_r, \mathrm{bio}, \mathrm{QA}). \quad (4)$$

In this procedure, relative values $v_A(k, \mathrm{bio}) = \delta_A(k, \mathrm{bio})/A_k$ and $v_r(k, i, \mathrm{bio}) = \delta_r(k, \mathrm{bio})/r_{k,i}$ were used to parameterize the overall uncertainties in the model and observations. Given relative uncertainties, the MISR LAI/FPAR algorithm approximates actual overall uncertainties as $\delta_A(k, \mathrm{bio}) =$

$v_A(k, \mathrm{bio})A_k$ and $\delta_r(k, i, \mathrm{bio}) = v_r(k, \mathrm{bio})r_{k,i}$, which are taken as the acceptable levels of uncertainties.

Fig. 8a–c shows RI(bio, QA), BI(bio, QA), and PI(bio, QA) for the optimal set of relative overall uncertainties (values listed in Tables 1 and 2). With the exception of broadleaf crops, the algorithm retrieves LAI values with a very high probability, if information about the biome type is available and uncertainties in input do not exceed the threshold acceptable level. The probability of identifying pure biome types is quite high if both tests were successfully executed, again with the exception of broadleaf crops (Fig. 8b, bars labeled "QA = 0"). If uncertainties in BRFs exceed the acceptable level and, as a consequence the second test fails, the probability of identifying grasses and cereal crops, shrubs, savannas, and broadleaf forests based on BHRs only is greatly reduced (Fig. 8b, bars labeled "QA = 1"). The first comparison test tends to extract information about canopy structure conveyed by the location of biome type in the spectral space. Although the locations of pure biome types in the spectral space are localized (Fig. 4d), the uncertainties in BHRs do not allow the algorithm to take full advantages of this property. Their effect is most pronounced in the case of spectrally similar biomes like broadleaf crops and savannas (Fig. 4d). Thus, the inclusion of additional angular information compensates for the loss of information due to uncertainties in input surface reflectances. Values of the BI corresponding to QA = 2 are higher compared to those derived from the first test only, with the exception of broadleaf crops and savannas (QA = 1). This suggests that the angular signature of vegetation conveys more information about the canopy structure than the location of BHRs in the spectral space, at least, for the data investigated here. However, as will be shown later in this paper, the use of BRFs only results in a lower retrieval quality, as compared to when the first test only or both tests are triggered to retrieve LAI values. This is because an increase in the amount of angular information not only increases the information content but also decreases the overall accuracy in the data. The former enhances quality of the retrievals, while the latter suppresses it. A failure of the algorithm to execute the first test indicates high uncertainties in BHR which, propagating through the surface retrieval algorithm, result in a poor quality of BRF

Table 2
Optimal values of relative uncertainties, v_r, in modeled and observed BRFs

View angle	Spectral band	Grass and cereal crops	Shrubs	Broadleaf crops	Savanna	Broadleaf forests
Nadir	Red	0.2	0.2	0.15	0.2	0.15
	NIR	0.2	0.2	0.05	0.2	0.05
Aa, Af	Red	0.2	0.15	0.15	0.2	0.15
	NIR	0.2	0.05	0.05	0.2	0.05
Ba, Bf	Red	0.2	0.2	0.225	0.2	0.225
	NIR	0.2	0.2	0.075	0.2	0.075
Ca, Cf	Red	0.2	0.2	0.3	0.2	0.3
	NIR	0.2	0.2	0.1	0.2	0.1
Da, Df	Red	0.2	0.2	0.45	0.2	0.45
	NIR	0.2	0.2	0.15	0.2	0.15

and, as a consequence, LAI retrievals. At the Langley ASDC, the operational version of the algorithm generates LAI and FPAR products only for the conditions of QA = 0 and QA = 1, i.e., the first or both comparison tests must be successful.

7. Impact of biome misidentification on LAI retrievals

Fig. 8c shows the PI for six biome types. On average, for only about 20% of pixels, both LAI and biome type can be simultaneously specified at the optimal level of uncertainties. This means that the majority of LAI values are retrieved using incorrect information about biome type. Table 3 summarizes disagreement between the biome types derived from the MISR LAI/FPAR algorithm and the six-biome map described earlier, as a function of QA. For a given vegetation type, the distribution of biomes assigned by the MISR algorithm is shown in rows. The aim of this section is to analyze the impact of biome misidentification on LAI retrievals.

To address this issue, we compare two LAI fields. The first, produced by the algorithm using the biome map as input, is taken as the reference field. The second LAI field was obtained by applying the MISR LAI/FPAR algorithm to the same data without using the biome map. For pixels in which both retrievals were available, a relative difference, Δ, was calculated between reference values, LAI_{ref}, and retrieved values, LAI_{MISR}, i.e.,

$$\Delta = \frac{LAI_{ref} - LAI_{MISR}}{LAI_{ref}}. \tag{5}$$

Pixels located around the data peaks (Fig. 4a) were used to generate these values. Fig. 9 shows histograms of Δ as a function of QA for different biome types. Mean values and standard deviations of Δ are shown in Table 4. With the exception of broadleaf crops and savannas, the impact of

biome misidentification on LAI retrievals is minimal if both comparison tests were executed (Table 4).

The histogram of Δ for shrubs corresponding to QA = 1 has two local minimums at $\Delta = 0$ and $\Delta = -0.7$ (Fig. 9). This biome was mainly misclassified as broadleaf forests and needleleaf forests (Table 3). The reference and retrieved LAI values for which the relative difference was close to -0.7 varied between 0.2 and 0.34, respectively. Shrubs exhibit lateral spatial heterogeneity, low to intermediate vegetation ground cover, and have a bright background. The information conveyed about the canopy structure is small and a wide range of natural variation in ground cover and soil brightness can result in the same value of the BHR. Broadleaf and needleleaf forests with a very low ground cover and bright (green) understory can result in similar values of surface reflectances at 1.1-km resolution. The effect of biome misclassification on the retrievals, therefore, is maximal if retrievals are from the first test only (curve "QA = 1" in Fig. 9b). The availability of additional angular information results in a reduced disagreement between reference and retrieved LAI values (curve "QA = 0" in Fig. 9b). Note that the probability of identifying shrubs using angular information only (QA = 2) is very high (Fig. 8b and Table 3). However, the inclusion of LAI retrievals corresponding to QA = 2 has no significant effect on the PI (Eq. (4) and Fig. 8a). Note that the failure of the algorithm to execute the first test (QA = 2) indicates high uncertainties in BHR which, propagating through the surface retrieval algorithm, result in poor quality BRFs, and, as a consequence, LAI retrievals.

For the other biome types, the disagreement between reference and retrieved LAI values is maximal for QA = 2 (Table 4). If retrievals are from the first or both comparison tests, the biome misidentification, on average, involves an overestimation of LAI for grasses and cereal crops and shrubs, and an underestimation in the case of broadleaf

Table 3
Disagreement between biome types assigned by the MISR algorithm and the six biome classification map used in the study for different values of QA

| Landcover type	QA	Landcover type assigned by MISR algorithm, %						
		Grasses and cereal crops	Shrubs	Broadleaf crops	Savannas	Broadleaf forests	Needleleaf forests	Failure
Grasses and cereal crops	0	81	7	4	1	0	0	7
	1	5.49	39.47	14.06	0	0	0	40.98
	2	29.94	14.48	0.08	0	8.5	35.19	11.81
Shrubs	0	0.03	38.33	0.91	0.01	13.91	3.37	43.44
	1	0	20	0	0	32	11	37
	2	0	100	0	0	0	0	0
Broadleaf crops	0	n/a	n/a	n/a	n/a	n/a	n/a	n/a
	1	0	2	69	0	0	29	0
	2	4	11	16	0.02	18	26	25
Savannas	0	42.7	3.3	9.5	37.2	0	6.7	0.6
	1	26	20	31	15	0	7	1
	2	n/a	n/a	n/a	n/a	n/a	n/a	n/a
Broadleaf forests	0	0	0	0	0	100	0	0
	1	0	0	0	77.5	12.5	0	10
	2	3.9	8.8	9.6	0	16	42.1	20
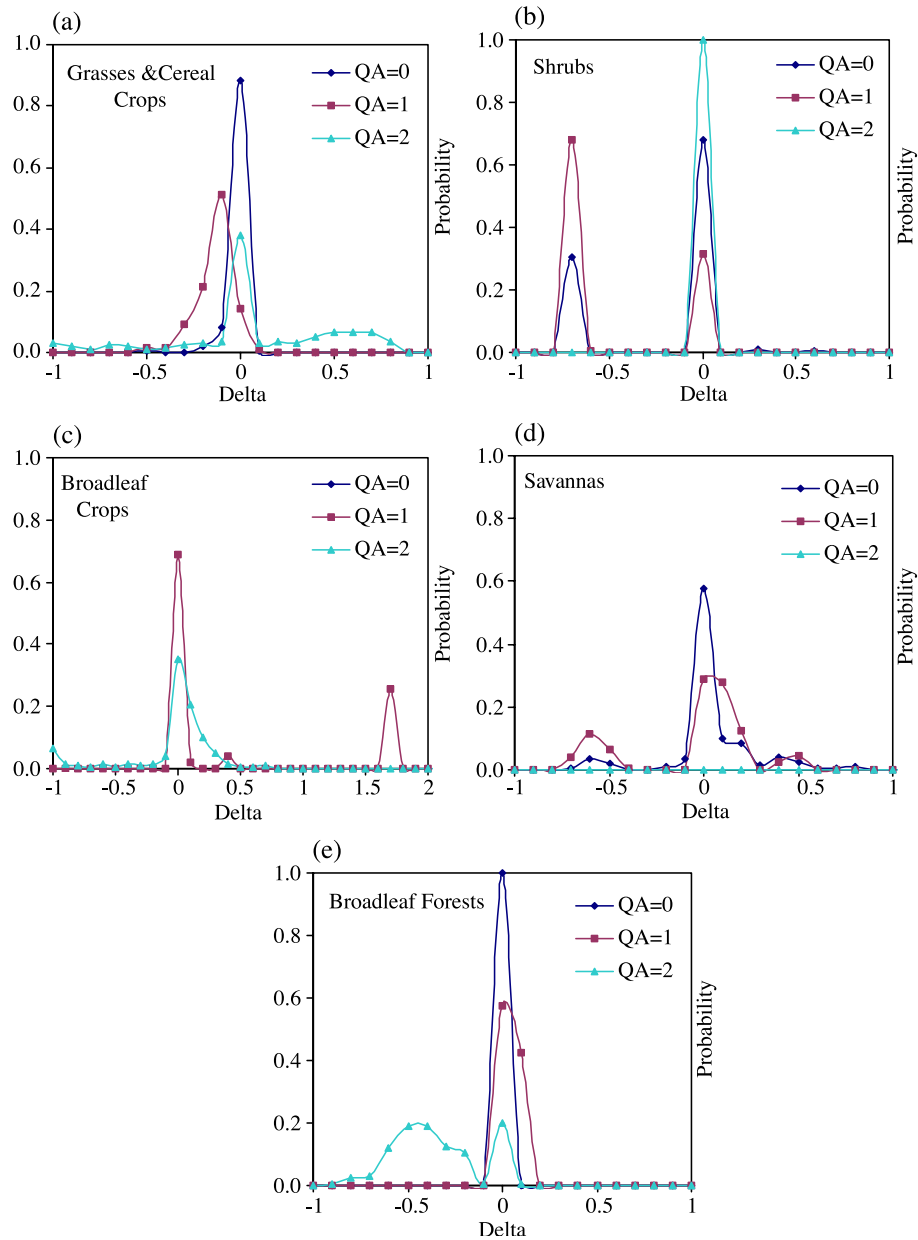
Fig. 9. Histograms of the relative difference between reference and retrieved LAI values for different biome types and QAs.

crops, savannas, and broadleaf forests (Fig. 9 and Table 4). In general, misclassification between distinct biomes has a significant effect on LAI retrieval. For example, shrubs are mainly misclassified as broadleaf or needleleaf forests (Table 3, QA = 1). The mean relative difference is − 0.37 compared to − 0.14 when the probability of such a mis-identification is much lower (Table 4, QA = 0).

What is the probability that biome misidentification has no impact on LAI retrieval? To address this question, we introduce the most probable relative difference as values of Δ at which the histogram exhibits local maxima. Many of histograms have two local maxima (Fig. 9), however, all biomes have a local maximum around $\Delta = 0$. Table 5 lists the most probable values of $\bar{\Delta}$ and probabilities of

$|\Delta - \bar{\Delta}| \leq \chi$ for different biome types, QA values, and disagreement levels χ.

For grasses and cereal crops, shrubs, savannas, and broadleaf forests, the disagreement between reference and high quality retrievals (QA = 0) does not exceed 15% with probabilities 97%, 68%, 71%, and 100%, respectively (Table 5). For 81% of savannas, the relative difference corresponding to QA = 0 and $\bar{\Delta} = 0$ is about 25%. With the exception of shrubs, more than 70% of intermediate quality retrievals agree with reference values to within 25%. For these retrievals, however, probabilities of $|\Delta| \leq 0.25$ are reduced. On average, with a probability of 70% and higher, the high and intermediate quality retrievals agree with true values to within 25% uncertainties, which is close to the

Table 4

Mean values and standard deviations of the relative difference for different biome types and QAs

	Mean			Standard deviation		
	QA = 0	QA = 1	QA = 2	QA = 0	QA = 1	QA = 2
Grasses and cereal crops	− 0.01	− 0.13	0.20	0.05	0.10	1.68
Shrubs	− 0.14	− 0.37	0	0.29	0.34	0.00
Broadleaf crops	n/a	0.45	0.60	n/a	0.73	3.03
Savannas	0.17	0.05	n/a	0.76	0.68	n/a
Broadleaf forests	0	0.04	− 0.35	0	0.05	0.22

overall uncertainty in model and observations (Tables 1 and 2). Thus, the optimal performance of the algorithm minimizes biome misclassification when it has a significant effect on LAI retrievals. With a very high probability, uncertainties due to the biome misclassification do not exceed uncertainties in model and observations.

Note that cover type information is an important input to LAI/FPAR algorithms that use single-angle observations. The typical overall accuracy in most biome maps is about 70% (Lotsch et al., 2003). Thus, about 30% of LAI retrievals should be treated as unreliable. The use of angular and spectral information of vegetations, instead of biome maps, results in comparable accuracy in LAI and also facilitates assignment of quality flags to retrievals. It should also be noted that uncertainties in the reference LAI field are unknown and thus the above analysis does not characterize uncertainties in retrievals. However, the proximity of retrieved and reference LAI fields indicates that MISR angular and spectral information is sufficient for LAI/FPAR retrievals without using land cover maps as input.

8. Test of physics

The measured spectral reflectance data are usually compressed into vegetation indexes. More than a dozen such indexes are reported in the literature and shown to correlate well with vegetation amount (Tucker, 1979), the fraction of
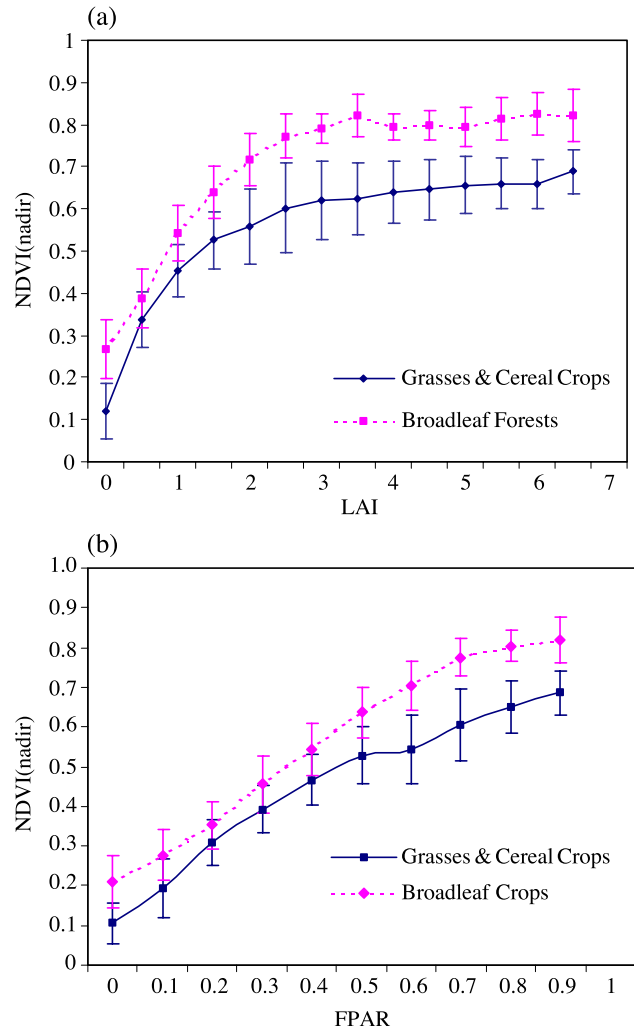

Fig. 10. (a) NDVI-LAI and (b) NDVI-FPAR regression curves for grasses and cereal crops and broadleaf forests, based on the MISR data. High quality retrievals (QA = 0) were used to derive these curves.

absorbed photosynthetically active radiation (Asrar, Fuchs, Kanemasu, & Harfield, 1984), unstressed vegetation conductance and photosynthetic capacity (Sellers, Berry, Col-

Table 5

Most probable values $\bar{\Delta}$ of the relative difference Δ and probabilities of $|\bar{\Delta} - \Delta| < \chi$ for different biome types, QAs, and disagreement levels χ

	Most probable value			Probability ($|\bar{\Delta} - \Delta| < \chi$)					
	QA = 0	QA = 1	QA = 2	QA = 0		QA = 1		QA = 2	
				$\chi = 0.15$	$\chi = 0.25$	$\chi = 0.15$	$\chi = 0.25$	$\chi = 0.15$	$\chi = 0.25$
Grasses and cereal crops	0	− 0.1	0	0.97	0.99	0.86	0.96	0.44	0.51
Shrubs	0	0	0	0.68	0.68	0.32	0.32	1	1
	− 0.7	− 0.7	–	0.32	0.32	0.68	0.68	–	–
Broadleaf crops	–	0	0	–	–	0.71	0.71	0.6	0.71
	–	0.4	–	–	–	0.04	0.04	–	–
	–	1.7	–	–	–	0.25	0.25	–	–
Savannas	0	0	–	0.71	0.81	0.57	0.7	–	–
	− 0.6	− 0.6	–	0.06	0.06	0.22	0.22	–	–
Broadleaf forests	0	0	0	1	1	1	1	0.2	0.3
	–	–	− 0.45	–	–	–	–	0.5	0.66

latz, Field, & Hall, 1992), and seasonal atmospheric carbon dioxide variations (Tucker & Sellers, 1986). There are some theoretical investigations to explain these empirical regularities (Knyazikhin, Martonchik, Myneni, Diner, & Running, 1998; Myneni, Hall, Sellers, & Marshak, 1995; Vygodskaya & Gorshkova, 1987). Such relationships provide a method to test the physics of retrievals. Here, we test relationships between the normalized difference vegetation index (NDVI), LAI, and FPAR. NDVI values were regressed against both LAI and FPAR to ascertain whether the proper relationships were obtained. The NDVI values were computed using the MISR nadir view HDRF values in the red and NIR bands. It should be emphasized that the LAI values were obtained from the MISR LAI/FPAR algorithm with MISR surface reflectances as inputs and not NDVI values. Fig. 10 shows the NDVI-LAI and NDVI-FPAR regression curves for grasses and cereal crops and broadleaf forests. The high quality retrievals (QA = 0) were used to derive these curves. The biome specific relationships between the retrieved LAI/FPAR and the

measured NDVI values conform to both theoretical and empirical results. Fig. 11 shows NDVI-LAI relationships for grasses and cereal crops and broadleaf forests corresponding to different values of QA. One can see that curves corresponding to QA = 2 do not follow regularities expected from physics and are mainly outside of the error bars of curves the NDVI-LAI relationships derived from high quality retrievals. A failure of the algorithm to execute the first test (QA = 2) indicates high uncertainties in BHR which, propagating through the surface retrieval algorithm, result in a poor quality of BRF, and, as a consequence, LAI retrievals. At the Langley ASDC, the operational version of the algorithm will generate LAI and FPAR products only for the condition of QA = 0 and QA = 1.

9. Concluding remarks

An algorithm for the retrieval of LAI, FPAR, and biome type from MISR BHR and BRF data has been in operational processing at the Langley ASDC since October 2002. This paper describes the research basis for transitioning the MISR LAI/FPAR product from beta to provisional status. The quality and spatial coverage of MISR surface reflectances input to the algorithm determine the quality and spatial coverage of the LAI and FPAR products. Therefore, our primary objective was to establish the convergence property of the MISR LAI/FPAR algorithm, namely, that the reliability and accuracy of the retrievals increase with increased input information content and accuracy.

The uncertainties in modeling the physics of the problem and measurements of surface reflectances are input to the MISR LAI/FPAR algorithm. An upper limit for these uncertainties that allows the algorithm to discriminate between pure biome types, minimize the impact of biome misidentification on LAI retrievals, and maximize the spatial coverage of retrievals was empirically evaluated from MISR data over Africa. Our analysis indicates that uncertainties in MISR BHR values over dense vegetation can substantially exceed the acceptable level of 20%, resulting in failure of the LAI/FPAR algorithm.

The performance of the MISR LAI/FPAR algorithm evaluated on a limited set of MISR data from Africa can be stated as resulting in valid LAI values and correct biome identification in about 20% of the pixels, on an average, given the current level of uncertainties in the MISR surface reflectance product. About 80% of LAI values are retrieved using incorrect information about biome type. We document that the LAI/FPAR algorithm minimizes biome misclassification when it has a significant effect on LAI retrievals. Finally, with a probability of about 70%, uncertainties in LAI retrievals due to biome misclassification do not exceed uncertainties in observations. These metrics will significantly improve as the quality of MISR surface reflectances improves. In fact, the surface reflectances used
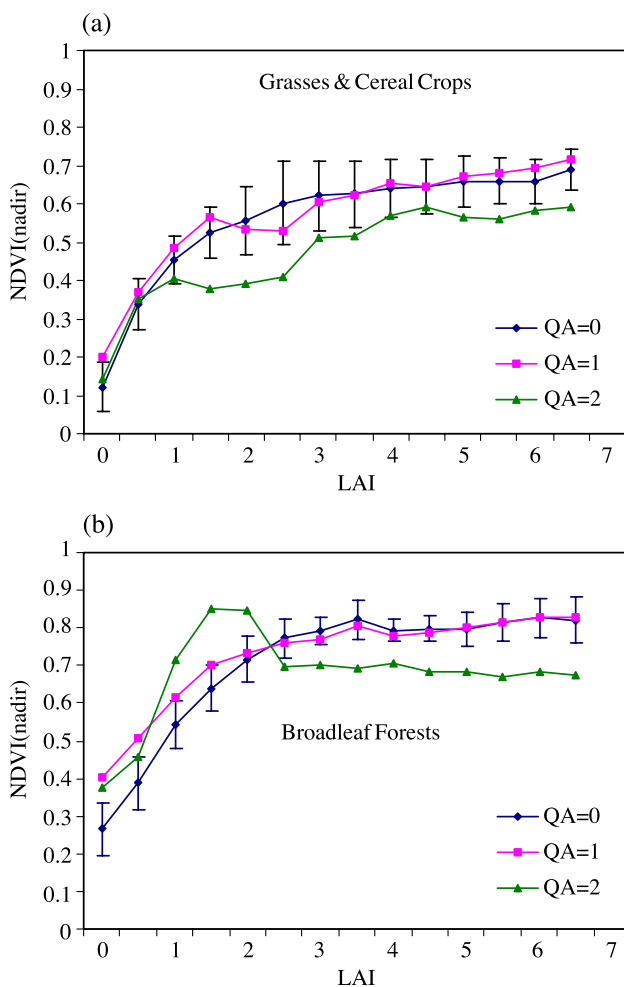

Fig. 11. NDVI-LAI regression curves for (a) grasses and cereal crops and (b) broadleaf forests for different values of QA.

in this article are already outdated, as the upstream algorithms and products, related to aerosol optical depth retrieval and atmospheric correction, have been significantly improved.

Considerable attention was also paid to characterizing the quality of the LAI/FPAR fields and this information is available to the users as quality assessment flags accompanying the product. A QA, as defined in this study, takes on values between 0 and 2, indicating that a retrieval passed both comparison tests (QA = 0, highest quality), the first test only (QA = 1, intermediate quality), or the second test only (QA = 2, low quality). Analyses presented in this paper indicate that, with a high probability, the quality indicator correctly reflects retrieval quality. Based on our investigation, one can conclude that the LAI/FPAR algorithm realizes the stated convergence goal, namely, that the reliability and accuracy of the retrievals increase with increased input information content and accuracy. Therefore, the increasing quality of the MISR surface reflectances will lead to better quality LAI and FPAR retrievals in the near future.

Nomenclature

ASDC	Atmospheric Sciences Data Center
BHR	Bihemispherical Reflectance
BI	Biome Identification Index
BRF	Bidirectional Reflectance Factor
CART	Canopy Architecture Radiative Transfer file
COVLAI	Coefficient of Variation of LAI
DAAC	NASA Distributed Active Archive Centers
DHR	Directional Hemispherical Reflectance
FPAR	Fraction of Photosynthetically Active Radiation absorbed by vegetation
HDRF	Hemispherical–Directional Reflectance Factors
LAI	Leaf Area Index
LaRC	Langley Research Center
LUT	Look-Up Table
MISR	Multi-angle Imaging SpectroRadiometer
MODIS	Moderate Resolution Imaging Spectroradiometer
NASA	National Aeronautics and Space Administration
NDVI	Normalized Difference Vegetation Index
NIR	Near Infra-Red
PI	Performance Index
QA	Quality Assessment
RI	Retrieval Index
SOM	Space Oblique Mercator projection

Acknowledgements

References

Asrar, G., Fuchs, M., Kanemasu, E. T., & Harfield, J. L. (1984). Estimating absorbed photosynthetic radiation and leaf area index from spectral reflectance in wheat. *Agron. J.*, *76*, 300–306.

Cohen, J. (1960). A coefficient of agreement for nominal scales. *Educational and Psychological Measurement*, *20*, 37–46.

Diner, D. J., Beckert, J. C., Reilly, T. H., Bruegge, C. J., Conel, J. E., Kahn, R. A., Martonchik, J. V., Ackerman, T. P., Davies, R., Gerstl, S. A. W., Gordon, H. R., Muller, J. P., Myneni, R. B., Sellers, P. J., Pinty, B., & Verstraete, M. M. (1998). Multi-angle Imaging SpectroRadiometer (MISR) instrument description and experiment overview. *IEEE Transaction on Geoscience and Remote Sensing*, *36*, 1072–1087.

Hansen, M., Defries, R., Townshend, J., & Sohlberg, R. (2000). Global land cover classification at 1 km spatial resolution using a classification tree approach. *International Journal of Remote Sensing*, *21*, 1331–1364.

Knyazikhin, Y., Martonchik, J. V., Diner, D. J., Myneni, R. B., Verstraete, M., Pinty, B., & Gobron, N. (1998). Estimation of vegetation canopy leaf area index and fraction of absorbed photosynthetically active radiation from atmosphere-corrected MISR data. *Journal of Geophysical Research*, *103*, 32239–32256.

Knyazikhin, Y., Martonchik, J. V., Myneni, R. B., Diner, D. J., & Running, S. W. (1998). Synergistic algorithm for estimating vegetation canopy leaf area index and fraction of absorbed photosynthetically active radiation from MODIS and MISR data. *Journal of Geophysical Research*, *103*, 32257–32274.

Lotsch, A., Tian, Y., Friedl, M. A., & Myneni, R. B. (2003). Land cover mapping in support of LAI and FAPAR retrievals from EOS-MODIS and MISR: Classification methods and sensitivities to errors. *International Journal of Remote Sensing*, *24*, 1997–2016.

Loveland, T. R., Merchant, J. W., Brown, J. F., Ohlen, D. O., Reed, B. C., Olsen, P., & Hutchinson, J. (1995). Seasonal land cover of the United States. *Annals of the Association of American Geographers*, *85*(2), 339–399.

Martonchik, J. V., Diner, D. J., Pinty, B., Verstraete, M. M., Myneni, R. B., Knyazikhin, Y., & Gordon, H. R. (1998). Determination of land and ocean reflective, radiative, and biophysical properties using multiangle imaging. *IEEE Transaction on Geoscience and Remote Sensing*, *36*, 1266–1281.

Myneni, R. B., Hall, F. G., Sellers, P. J., & Marshak, A. L. (1995). The interpretation of spectral vegetation indexes. *IEEE Transaction on Geoscience and Remote Sensing*, *33*, 481–486.

Myneni, R. B., Hoffman, S., Knyazikhin, Y., Privette, J. L., Glassy, J., Tian, Y., Wang, Y., Song, X., Zhang, Y., Smith, G. R., Lotsch, A., Friedl, M., Morisette, J. T., Votava, P., Nemani, R. R., & Running, S. W. (2002). Global products of vegetation leaf area and fraction absorbed PAR from year one of MODIS data. *Remote Sensing of Environment*, *83*, 214–231.

Myneni, R. B., Nemani, R. R., & Running, S. W. (1997). Estimation of global leaf area index and absorbed par using radiative transfer models. *IEEE Transaction on Geoscience and Remote Sensing*, *35*, 1380–1393.

Panferov, O., Knyazikhin, Y., Myneni, R. B., Szarzynski, J., Engwald, S., Schnitzler, K. G., & Gravenhorst, G. (2001). The role of canopy structure in the spectral variation of transmission and absorption of solar radiation in vegetation canopies. *IEEE Transaction Geoscience and Remote Sensing*, *39*(2), 241–253.

Privette, J. L., Myneni, R. B., Knyazikhin, Y., Mukelabai, M., Roberts, G., Tian, Y., Wang, Y., & Leblanc, S. G. (2002). Early spatial and temporal validation of MODIS LAI product in the southern Africa Kalahari. *Remote Sensing of Environment*, *83*, 232–243.

Sellers, P. J., Berry, J. A., Collatz, G. J., Field, C. B., & Hall, F. G. (1992). Canopy reflectance, photosynthesis and transpiration. III: A reanalysis using improved leaf models and a new canopy integration scheme. *Remote Sensing of Environment*, *42*, 1–20.

Shabanov, N. V., Wang, Y., Buermann1, W., Dong, J., Hoffman, S., Smith, G. R., Tian, Y., Knyazikhin, Y., & Myneni, R. B. (2003). Effect of

foliage heterogeneity on the MODIS LAI and FPAR over Broadleaf Forests. *Remote Sensing of Environment* (in press).

Tian, Y., Wang, Y., Zhang, Y., Knyazikhin, Y., Bogaert, J., & Myneni, R. B. (2001). Radiative transfer based scaling of LAI/FPAR retrievals from reflectance data of different resolutions. *Remote Sensing of Environment*, *84*, 143–159.

Tian, Y., Woodcock, C. E., Wang, Y., Shabanov, N. V., Privette, J. L., Zhou, L., Knyazikhin, Y., Veikkanen, B., Hame, T., Buermann, W., Dong, J., Ozdogan, M., & Myneni, R. B. (2002a). Multiscale analysis and validation of MODIS LAI product over Maun, Botswana. I: Uncertainty assessment. *Remote Sensing of Environment*, *83*, 414–430.

Tian, Y., Woodcock, C. E., Wang, Y., Shabanov, N. V., Privette, J. L., Zhou, L., Knyazikhin, Y., Veikkanen, B., Hame, T., Buermann, W., Dong, J., Ozdogan, M., & Myneni, R. B. (2002b). Multiscale analysis and validation of MODIS LAI product over Maun, Botswana. II: Sampling strategy. *Remote Sensing of Environment*, *83*, 431–441.

Tucker, C. J. (1979). Red and photographic infrared linear combination for monitoring vegetation. *Remote Sensing of Environment*, *8*, 127–150.

Tucker, C. J., & Sellers, P. J. (1986). Satellite remote sensing of primary production. *International Journal of Remote Sensing*, *7*, 1395–1416.

Wang, Y., Buermann, W., Stenberg, P., Smolander, H., Häme, T., Tian, Y., Hu, J., Knyazikhin, Y., & Myneni, R. B. (2003). A new parameterization of canopy spectral response to incident solar radiation: Case study with hyperspectral data from pine dominant forest. *Remote Sensing of Environment* (in press).

Wang, Y., Tian, Y., Zhang, Y., El-Saleous, N., Knyazikhin, Y., Vermote, E., & Myneni, R. B. (2001). Investigation of product accuracy as a function of input and model uncertainties: Case study with SeaWiFS and MODIS LAI/FPAR algorithm. *Remote Sensing of Environment*, *78*, 299–313.

Vygodskaya, N. N., & Gorshkova, I. I. (1987). *Theory and experiment in vegetation remote sensing* (p. 248). St. Petersburg, Russia: Gidrometeoizdat, in Russian, with English abstract.

Zhang, Y., Shabanov, N., Knyazikhin, Y., & Myneni, R. B. (2002). Assessing the information content of multiangle satellite data for mapping biomes II: Theory. *Remote Sensing of Environment*, *80*, 435–446.